Noname manuscript No.
doi.org/10.1007/s13239-021-00570-7

Semi-Automatic Reconstruction of Patient-Specific Stented Coronaries based on Data Assimilation and Computer Aided Design

Adrien Lefieux · Sara Bridio · David Molony · Marina Piccinelli · Claudio Chiastra · Habib Samady · Francesco Migliavacca · Alessandro Veneziani

Received: 1 February 2021 / Accepted: 26 July 2021

Abstract *Purpose.* The interplay between geometry and hemodynamics is a significant factor in the development of cardiovascular diseases. This is particularly true for stented coronary arteries. To elucidate this factor, an accurate patient-specific analysis requires the reconstruction of the geometry following the stent deployment for a computational fluid dynamics (CFD) investigation.

Some of the computation were performed on XSEDE facilities (Stampede 2) under the NSF-XSEDE TG-ASC160069 Grant. H. S. acknowledges the support to his research from Medtronic, Abbott Vascular, Philips, Gilead.

A. Lefieux
Department of Mathematics, Emory University, Atlanta, GA USA, Department of Medicine (Cardiology), Emory University Hospital, Atlanta, 30322 GA USA. E-mail: alefieu@emory.edu, Present E-mail: adrien.lefieux@gmail.com

S. Bridio
Laboratory of Biological Structure Mechanics (LaBS), Department of Chemistry, Materials and Chemical Engineering "Giulio Natta", Politecnico di Milano, Milan 20133 IT

D. Molony
Department of Medicine (Cardiology), Emory University Hospital, Atlanta, 30322 GA USA

M. Piccinelli
Department of Radiology, Emory University Hospital, Atlanta, 30322 GA USA

C. Chiastra
PoliTo^{BIO}Med Lab Department of Mechanical and Aerospace Engineering, Politecnico di Torino, Turin 10129 IT

H. Samady
Department of Medicine (Cardiology), Emory University Hospital, Atlanta, 30322 GA USA

F. Migliavacca
Laboratory of Biological Structure Mechanics (LaBS), Department of Chemistry, Materials and Chemical Engineering "Giulio Natta", Politecnico di Milano, Milan 20133 IT

A. Veneziani
Department of Mathematics, Department of Computer Science, Emory University, Atlanta, GA 30322 USA

Post-print

The image-based reconstruction is troublesome for the different possible positions of the stent struts in the lumen and the coronary wall. However, the accurate inclusion of the stent footprint in the hemodynamic analysis is critical for detecting abnormal stress conditions and flow disturbances, particularly for thick struts like in bioresorbable scaffolds. Here, we present a novel reconstruction methodology that relies on Data Assimilation and Computer Aided Design.
Methods. The combination of the geometrical model of the undeployed stent and image-based data assimilated by a variational approach allows the highly automated reconstruction of the skeleton of the stent. A novel approach based on computational mechanics defines the map between the intravascular frame of reference (called L-view) and the 3D geometry retrieved from angiographies. Finally, the volumetric expansion of the stent skeleton needs to be self-intersection free for the successive CFD studies; this is obtained by using implicit representations based on the definition of Nef-polyhedra.
Results. We assessed our approach on a vessel phantom, with less than 10% difference (properly measured) vs a customized manual (and longer) procedure previously published, yet with a significant higher level of automation and a shorter turnaround time. Computational hemodynamics results were even closer. We tested the approach on two patient-specific cases as well.
Conclusions. The method presented here has a high level of automation and excellent accuracy performances, so it can be used for larger studies involving patient-specific geometries.

Keywords Optical Coherence Tomography · Stent · Image analysis · Image Processing

Post-print

1 Introduction

Percutaneous Coronary Intervention (PCI) is a common minimally invasive procedure to treat diseased coronary arteries [4]. It consists of the mechanical restoration of the stenotic lumen through balloon expansion (i.e., balloon angioplasty) followed by the deployment of a metallic tubular mesh, known as *stent*. The major issues related to stent placement are in-stent restenosis and thrombosis. These adverse clinical events seem to be promoted by the abnormal flow patterns induced by the presence of the stent [48,44,57].

Since flow patterns measures are difficult in vivo, numerical modeling, in particular Computational Fluid Dynamics (CFD), is a valuable tool for quantification [11]. The step-like geometry introduced by the stent in the flow stream majorly affects the local hemodynamics, not to mention the perturbation induced by the floating ("malapposed") stent struts [10]. Accurate quantification of this interplay may help to understand in-stent restenosis and thrombosis. On a longer-term, it may support the prediction of adverse events and the design of next-generation endovascular devices. To do this, the reconstruction of patient-specific stented lumens is necessary. Patient-specific studies focusing on the artery scale only - without the stent footprint - may

help only at a qualitative level, since specific *local* geometrical features (e.g., at the level of the struts) do affect the hemodynamics significantly.

The significance of computational studies for the clinical purpose is related to the number of patients that numerical modeling tools can realistically process. It is critical that numerical models can be used over a large number of patients, enough for clinical trials, in the frame of the so-called "*In Silico*" or "Computed-Aided Clinical Trials." A merit criterion for the design of a workflow, beyond accuracy and reliability, is therefore the high level of automation necessary for the efficiency and the operator-independence. While CFD models for hemodynamics and automatic or semi-automatic methods for the unstented lumen reconstruction are well established (see, e.g., [2,20,59]), automatic (and reliable) stent reconstruction methods are not available. In more detail, in [11,38,36,37,61] most of the stented vessel geometry reconstruction steps requires significant operator interventions, in particular regarding stent/lumen co-registration and stent mesh repair. Automation procedures may rely essentially on two different paradigms: i) the "*model-driven*" approach, where the entire stent deployment procedure is simulated to identify the final post-operative vessel geometry [14]; ii) the "*data-driven*" approach [22], where the stented geometry is retrieved from images. Most of the approaches collocate between these two paradigms, combining physical or geometrical models with the available data [11,18,45].

In the "data-driven" approaches, images obtained from Optical Coherence Tomography (OCT) are the best candidate for a high-fidelity reconstruction. OCT is an intravascular imaging technique, from which a series of high-resolution cross-sectional images of the stented lumen is obtained during a catheter pullback (in-plane axial commercially available resolution of 12 - 15 μm, in-plane lateral resolution of 20 - 40 μm, interframe distance of 100 - 200 μm) [43]. As with any intravascular imaging, the real 3D positioning of the vessel in space cannot be retrieved. Indeed, from OCT, an almost rectilinear[1] cylindrical stack of images, called *L-view*, is obtained. We need extra-vascular imaging to retrieve the real positioning in space with the actual vessel centerline. Usually, two angiographic views are combined with OCT images to obtain the 3D patient-specific topology of the stent [11,31].

We propose here a method to reconstruct patient-specific stented coronary arteries based on Data Assimilation and Computer Aided Design. The *assimilation of data and models* is done at the morphological level, by combining the position of the stent struts detected on the images (the "foreground" information) and the topology of the stent wireframe in undeployed conditions (the "background" information available from the stent manufacturer and independent of the specific patient), via a *polyline-to-point cloud registration* (skeletonization process) [32]. The skeleton or volumetric stent medial axis is represented by a polyline, i.e. a set of piecewise linear curves. The polyline is then registered onto the OCT segmented point-cloud corresponding to the stent struts by solving an inverse problem. The volumetric reconstruction is then accom-

[1] Deviations from rectilinear are induced by the catheter floating.

Post-print

plished by using Nef-polyhedra [25], to guarantee the topological quality of the reconstructed stent mesh. All the steps proposed are intended to go beyond a proof-of-concept and, in the follow-up of the present work, designed to be almost operator-independent and (semi-)automatic, by using state-of-the-art computational geometry technique. This enables a short turnaround time to deliver the mesh used in CFD.

The proposed pipeline shares some features with other available approaches in the literature [36,61,45,12,60]. We differ for the specific image-registration procedure during the skeletonization phase (Sect. 2.2.2), the combination between intra and extravascular images (Sect. 2.2.2) and the volume sweeping procedure (Sect. 2.2.3). The lumen and the stent are reconstructed as separate items; successively, the stent is subtracted from the lumen to create the footprint in the final geometrical reconstruction.

In addition to the reconstruction method (Sect. 3.1), for benchmarking we report some results of CFD simulations (Sect. 3.2) pointing out the reliability and efficiency of our approach when evaluating the local hemodynamics in the stented region. We use standard CFD methods, even if specific features of blood flow around the struts requires *ad hoc* stabilization techniques [55]. However, the CFD methodology is not the focus of the present paper.

The results are discussed in Sect. 4, while we draw our conclusive statements in Sect. 5.

2 Materials and Methods

2.1 Benchmark Data Collection

First, the proposed method was tested with a Multi-Link 8 stent (Abbott Vascular, Santa Clara, CA, USA), a metallic stent implanted in a realistic coronary artery phantom designed and 3D printed [36] (Fig. 1). OCT images were acquired on the phantom for the stented lumen reconstruction with an inter-frame spacing of 100 μm. Besides, micro-computed tomography (μCT) images were acquired using the C7-XR OCT system (St. Jude Medical, St. Paul, MN, USA) to reconstruct the vessel centerline [36]. This experimental investigation allowed evaluating the accuracy of the skeletonization in a case free of image artifacts like those occurring in a routine *in vivo* acquisition. In this test, we used the original approach in [36] as *ground truth* (very accurate and time-consuming) to assess the impact of the different reconstruction methods on the local hemodynamics.

Then, the proposed method was applied to two patient-specific cases provided by Emory University Hospital (Atlanta, GA, USA). The implanted stents were both bioresorbable Absorb GT1 Bioresorbable Vascular Scaffolds (Abbott Vascular) (Fig. 2). The two cases are labeled as BVS1 and BVS2. OCT images were acquired with an inter-frame spacing of 250 μm for the BVS1 case and 200 μm for the BVS2 case. BVS1 and BVS2 were implanted in a straight and a curved coronary track, respectively. Polylines for the skeleton of

Post-print

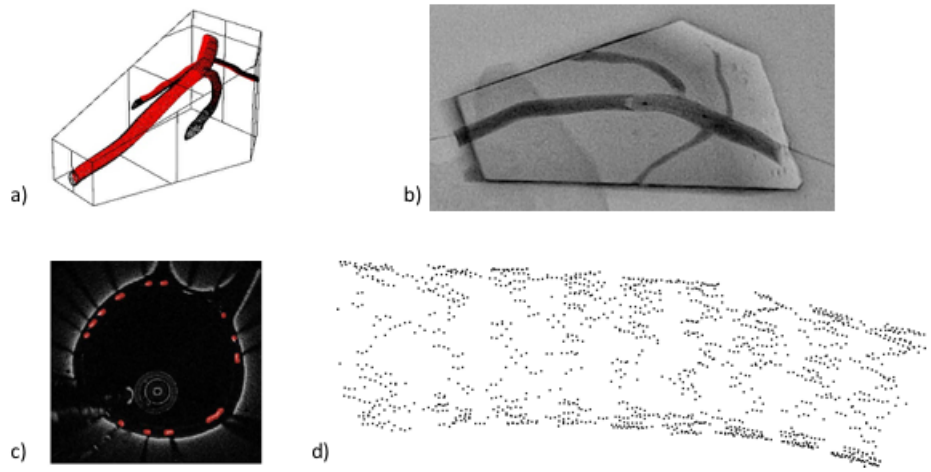

Fig. 1 a) CAD model of the coronary artery phantom for 3D printing; b) angiographic image of the 3D printed phantom after stent implantation; c) example of segmented OCT frame, with highlighted stent strut sections (red); d) point cloud resulting from OCT image segmentation and 3D space mapping according to μCT images (see Migliori et al. [36] for further details).

the undeployed stent can be extracted from either scanned geometries using μCT [36] or from the manufacture's CAD model. Possible methodologies for the extraction from polyhedra are described for instance in [54]. For the patient-specific cases considered here, these polylines are retrieved from the manufacturer's CAD model. We picked on purpose these two cases featuring a different coronary curvature to illustrate our approach on diverse cases. We compared the CFD with the local hemodynamics in the same lumen geometries without stent (i.e., unstented lumen), to point out the importance of the stent footprint.

It is worth noting that the proposed method readily extends to different stent platforms, as long as the stent template is available. The only restriction is that the stent cross-section has to be convex (like for circular or rectangular sections), as we motivate later on for the volumetric reconstruction.

Post-print

2.2 Reconstruction method of stented vessels

The *reconstruction of the coronary lumen*, without the footprint of the stent, is based on a semi-automatic standard procedure, which relies on the level-set method [53]. This process is performed with an in-house Python code based on the VTK library [51]. In our experience, OCT pullbacks with the current technology may generate artifacts [46] that undermine the robustness of the segmentation process. In this case, manual corrections are necessary.

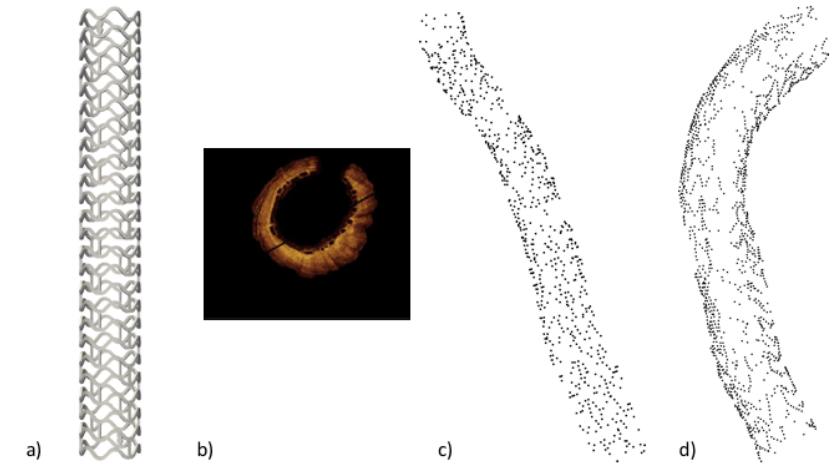

Fig. 2 a) CAD model of an Absorb GT1 Bioresorbable Vascular Scaffolds (BVS) (Abbott Vascular) in its undeformed configuration before the crimping process; b) example of processed OCT frame (the BVS strut sections appear as dark boxes); point cloud resulting from OCT image segmentation and 3D space mapping according to angiographic images for BVS1 (c) and BVS2 (d), respectively (see [61] for further details).

As described below, the *reconstruction of the stent* consists of three major steps: i) stent strut detection on the images, ii) skeletonization by registration and mapping in 3D, and iii) reconstruction by volume sweeping.

2.2.1 Stent strut detection

The stent struts were detected in the acquired OCT images using the segmentation method for metallic stents described in [12,36] for the Multi-Link 8 stent geometry (Fig. 1c) and that for polymeric stents described in [61] for the BVS1 and BVS2 scaffold geometries (Fig. 2b), respectively. The resulting stent struts point clouds were used as input for the novel stent skeletonization method.

2.2.2 Skeletonization

The stent strut detected in the OCT images are successively stacked to obtain a cloud of sparse points, with no topology encoded. The topology, (i.e., the map of nodes and edges of the stent frame the points belong to), is hardly encoded from OCT images, as the catheter can float/rotate during the pullback and the entire slice in each image is not visible for the presence of the guidewire shadow.

Manual stent topology reconstruction is sub-optimal [61], and it shows a high operator dependence. A possible automatic approach is given by the NN-Crust algorithm [16]. Unfortunately, its performances heavily depend on the

Post-print

density of the point cloud, which is a function of the pullback speed and the heart motion in our application; hence, it is expected to be highly variable in clinical applications. Therefore, we opted for a Data Assimilation procedure where the undeployed design of the stent is the model to retrieve the topology on the cloud of points. To achieve this task rigorously, we need to register the skeleton of the undeployed stent and the points. This calls for a *polyline-to-points registration*. While surface-to-surface or polyline-to-polyline registration is a well-investigated topic, polyline-to-point is less developed. Before we recall the specific solution of the inverse problem required by the registration procedure, we notice that we have two options in our workflow. As we mentioned in the introduction, the OCT data refer to the L-view, i.e. the frame of reference of the intravascular imaging. The real 3D location is retrieved from the angiographies. We have therefore two steps: the image registration and the 3D map. At this stage, two options are available[2]: **Map-then-Register** (MR), where we first use the extra-vascular imaging to get the positions of the struts in the real 3D patient frame-of-reference and then we find the topology by registration (see [45,32]); **Register-then-Map** (RM), where we apply the registration in the L-view framework, and then we find the map to the 3D space (Fig. 3).

Conceptually, the map is just a change of reference (forward problem), while the registration is an optimization step (inverse problem). Albeit the two steps theoretically should commute, from the algorithmic viewpoint the two options are different. Hereafter, we focus primarily on the RM workflow, as this will be our choice. However, the descriptions of the two steps (forward and inverse) are general enough to infer the MR approach as well. We motivate our choice for RM in the Discussion.

L-view polyline-to-point-cloud registration. Registration consists in finding the transformation that makes an object called *template* similar to an object called *reference* [39]. In our case, the template is a polyline representing the skeleton of the *undeformed* stent design. *Vertices* and *edges* define a polyline. An *edge* is a couple of connected *vertices*. The reference of the registration is the OCT-derived strut-point cloud (Fig. 3, leftmost panel). The result is a function applied to the vertices of the polyline while the connectivity remains unaltered, that minimizes the distance between the deformed template and the reference. This is the solution of a variational (minimization) problem, that we perform in a deterministic sense, i.e. with no specific assumption on the probabilistic nature of the noise affecting the data (the reference). We limit ourselves to recalling the basic features of our assimilation procedure, a complete description can be found in [32]. More precisely, the assimilation of the data and the model is obtained by minimizing the following functional

$$\text{find } \boldsymbol{y} \text{ to minimize} : D(\boldsymbol{y}, \boldsymbol{p}) + \alpha S(\boldsymbol{y}) \tag{1}$$

where $\boldsymbol{y}$ is the deformed polyline (i.e. the image of the polyline according to the unknown map), $\boldsymbol{p}$ is the OCT-derived strut-point cloud, D is a measure

[2] To the best of the authors' knowledge, the terminology that follows has not used elsewhere.

Post-print

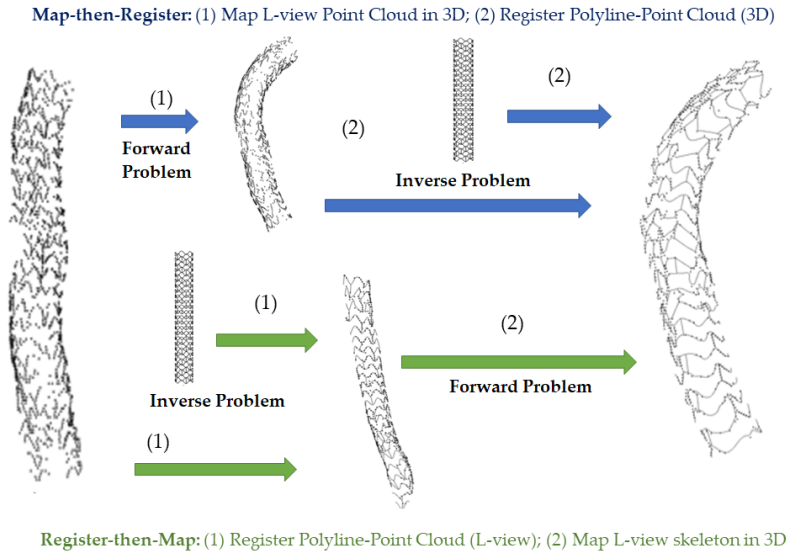

Fig. 3 Strategies for stent skeletonization: Map-then-Register (MR), top vs. Register-then-Map (RM), bottom. MR follows the upper blue arrows: the registration is performed by fitting the undeployed stent skeleton to the 3D stent strut point cloud. RM follows the green arrows: polyline-to-point-cloud registration by fitting the skeleton to the L-view stent strut point cloud and then map of the resulting polyline to the 3D space.

of the geometrical mismatch between the polyline and the point cloud, while S is a so-called *regularizer* that reduces unphysical deformations of the polyline. Technically speaking, the latter term helps the mathematical procedure to obtain a reasonable solution ("convexification" of the problem), by possibly incorporating physical constraints that help preventing the calculation of inconsistent minima [39]. In [32], a non-parametric regularization procedure is specifically proposed for a stent-registration problem. This non-parametric regularizer is composed of two terms: a "diffusion" one, to smooth the deformation, and a term that penalizes the stretching deformation. The regularization parameter $\alpha > 0$ balances the weight of these constraints in the minimization, and it can be empirically determined [19]. Specifically, we opted for the well-known L-curve criterion as implemented in the Matlab library FAIR [40]. To obtain good results with the non-parametric regularizer, a good initial guess is required. In [32], an affine transformation followed by a non-linear hyper-elastic deformation is proposed. Note that Coherent Point Drift (CPD) [42] can be used as well.

We selected the mismatch measure as the sum-of-squared-distance (SSD) function

$$D^{SSD}(\boldsymbol{y},\boldsymbol{p}) = \frac{1}{2}||\boldsymbol{q}(\boldsymbol{y}) - \boldsymbol{p}||^2 = \frac{1}{2}\sum_{i=1}^{N}\Big[(q_x(\boldsymbol{y}) - p_x)^2 + (q_y(\boldsymbol{y}) - p_y)^2 + \kappa\,(q_z(\boldsymbol{y}) - p_z)^2\Big] \tag{2}$$

Post-print

where $\boldsymbol{q}(\boldsymbol{y})$ is a vector $[q_x, q_y, q_z]$ containing the projections of the points $\boldsymbol{p}$ (with coordinates $[p_x, p_y, p_z]$) onto the edges of the deformed polyline and κ is a real number. The map of the polyline deformation is parametrized to minimize this distance. The parameters used for the deformation function are the coordinates of the vertices of the polyline. Consequently, the size of the problem (i.e., the size of the associated linear system) is driven by the number of vertices of the polyline, as we are considering piecewise linear polylines. Longer stents, or stents with complex geometries that require finer discretization, will result in larger problems. In our problems, the number of points is in the range $(10^3, 10^4)$.

Problem (1,2) defines our specific deterministic variational assimilation procedure. It is substantially different from other approaches like the one in [45], where the assimilation is performed directly on the OCT and the angiographies and not on the skeleton-point cloud pair. In [32] only the case $\kappa = 1$ was considered. The introduction of this parameter is a novel contribution of the present work.

For $\kappa = 1$, (2) is *isotropic* (i.e., all the directions are treated at the same way). This is, however, is inconsistent with the different density of points and the different levels of noise affecting the images (and consequently, the coordinates of the points retrieved from the OCT). More precisely, the density of points along the in-plane coordinates (x and y in the L-view) is generally much higher than along the longitudinal (z in the L-view) direction. Considering that the longitudinal resolution is between 0.1 and 0.2 mm, while in each frame, we have a point with a linear density of about 0.01 mm [29], the D^{SSD} definition (2) addresses this anisotropy. OCT images are noisier along the longitudinal direction than in the cross-sectional planes. Indeed, the in-plane noise due to the cardiac motion is small, at a frame rate of 100 frame/s in the current OCT platforms, compared to the noise due to the relative cardiac motion in the longitudinal direction with a pullback speed of about 10-40 mm/s [29,56]. Notice that the longitudinal resolution (and thus the point cloud density in z) is primarily a function of the sampling rate and the pullback speed. Current commercial vendors have a sampling rate of from 100 to 160 frame/s, with a pullback speed between 10 to 40 mm/s [24]. The longitudinal frame density is then defined as the ratio of frame acquisition rate by the pullback speed. For a constant frame acquisition rate, lowering the pullback speed would increase the frame density, but it would increase the signal-to-noise (SNR) ratio as the pullback would span additional cardiac cycles.

Based on these considerations, with the weight κ along the z coordinate[3] we introduced in the L-view an anisotropic treatment of the data. The selection of the parameter κ is not trivial, as it should be a trade-off between the different density of points (that suggests to take $\kappa > 1$ to balance the fewer data along z) and the different SNR ratio (that suggests to take a smaller κ to balance the impact of the noise on the minimization). Therefore, enforcing a larger κ improves the absolute value of the minimization (we obtain smaller values of D^{SSD}), but it may lead to an unphysical solution for the presence of the noise.

[3] Here, we have no reason for introducing different parameters for the in-plane Cartesian coordinates x and y. A different coordinate system (e.g., polar) may require different parameters.

Post-print

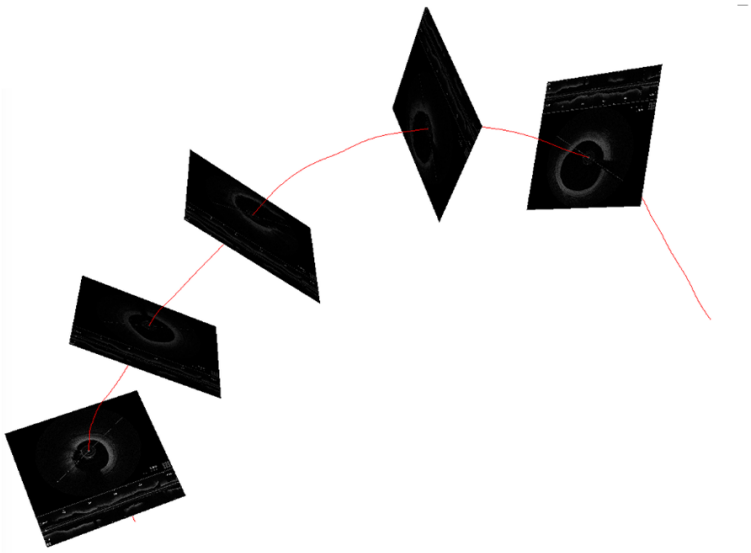

Fig. 4 Positioning of the OCT frames on the centerline reconstructed from the angiographies.

The optimal κ depends on the acquisition, the pullback velocity, and the SNR, which are case-dependent. Recent findings on OCT techniques resort to high sampling rates [15,28], which may be well corresponded by isotropic mismatch measures ($\kappa = 1$). However, for current commercial solutions, an anisotropic metric seems more appropriate. For example, considering that the in-plane resolution is 0.01 mm, and the longitudinal resolution is 0.1 mm, we might set $\kappa = 10$. We discuss the sensitivity on this parameter in the Discussion.

It is worth stressing that an anisotropic distance is possible only in the L-view, where the different resolutions occur along with the different Cartesian directions. This is a crucial point in favor of RM, since, in the MR approach, this differentiation is not possible, as we discuss later on.

Mapping to the 3D space The identification on the angiographic images of the 3D path of the wire within the vessel was routinely performed with QAngio XA 3D RE (Medis Medical Imaging Systems, Leiden, The Netherlands). Once the wire trajectory is available, frames retrieved from the OCT can be positioned perpendicularly to it, mimicking the way they were acquired, while retaining the exact 3D orientation, Fig. 4.

A common anatomical landmark is needed as a starting point to register all the images at the correct location along the reconstructed wire trajectory. The landmark is usually a bifurcation that can be identified on both the angiographies and the OCT images stack. Once this correspondence has been

Post-print

established, all frames can be positioned along the wire, before and after the landmark, at the proper inter-frame distance.

The registration of each image is performed by computing the point-wise Frenet frame of the line representing the wire 3D trajectory. The Frenet (or Tangential-Normal-Binormal) frame is a common way to provide a coordinate system for each point of a 3D line. Formally, the computation of the Frenet frame requires C^3-regularity of the centerline equation, that can be achieved by resorting to fourth-degree splines (see, e.g., [50]).

Each image is subsequently registered to the corresponding point on the 3D wire and perpendicular to it so that the tangent vector of the line is normal to the image plane. The mapping of each frame in 3D is formalized through a roto-translation described by a 4×4 matrix R defined as

$$R = \begin{bmatrix} A & \mathbf{b} \\ \mathbf{0} & 1 \end{bmatrix} \tag{3}$$

where the 3×3 block-matrix A is the rotation matrix (orthogonal matrix, i.e., $A^T = A^{-1}$), and the 3×1 vector $\mathbf{b}$ is the translation vector. The coordinates of each point in an OCT frame plane are multiplied by the corresponding matrix to obtain the coordinates of the mapped points.

In the RM paradigm, this procedure is applied to the polyline resulting from L-view registration. This maps the stent skeleton into the 3D space. *This step has some nontrivial aspects to address.* In general, the polyline vertexes do not belong to the OCT frame planes. On the other hand, the mapping information is only available for those planes extracted from the images. We need therefore to extend the map from the OCT planes to the entire 3D space.

Our approach relies on the simulation of a physical deformation. This is not used for the computation of the real deployment, but only for extending the map available in only a restricted number of positions to the entire 3D space, consistent with the physics of the problem. We deform the entire L-view space that contains the registered stent polyline by virtually embedding it into a stack of elastic cylinders. Each cylinder is defined as having the bases corresponding to two adjacent OCT frame-planes. Then, it is meshed with tetrahedral elements with a Delaunay algorithm and an element size of 0.6 mm (using Gmsh [21]). This is a trade-off between accuracy and efficiency. We tried 0.2 mm with no significant change in the results.

The configuration after the cylinder creation is shown in Fig. 5a. The stack of cylinders is then mapped to the 3D space by applying a linear elastic transformation to each cylinder. The mapping is accomplished with a specific solver written in the Python library FEniCS [1]. The Dirichlet boundary conditions for the elasticity problem are obtained by the maps of the OCT slices retrieved from the roto-translation matrices. Formally, this means that we solve the following problem in the cylindrical region Ω_L wrapping the point cloud (Fig. 5a):

$$\nabla \cdot \left(\lambda(\nabla \cdot \mathbf{u})\boldsymbol{I} + 2\mu\left(\nabla\mathbf{u} + \nabla\mathbf{u}^T\right)\right) = 0 \tag{4}$$

Post-print

where $\boldsymbol{I}$ is the identity tensor and $\mathbf{u}$ is the deformation. The Lame's constants λ and μ are related to the Young's Modulus E and the Poisson ratio ν of the continuum by the classical relations

$$\lambda = \frac{\nu E}{(1+\nu)(1-2\nu)},\ \mu = \frac{E}{2(1+\nu)}. \tag{5}$$

Equation (4) is solved for each cylinder and is completed by the boundary conditions ($\mathbf{n}$ is the unit outward normal vector to the boundary)

$$\begin{cases} \mathbf{u} = RT(OCT) & \text{(basis)}, \\ \lambda(\nabla \cdot \mathbf{u})\mathbf{n} + \left(2\mu\left(\nabla \mathbf{u} + \nabla \mathbf{u}^T\right)\right) \cdot \mathbf{n} = \mathbf{0} & \text{(lateral surface)}. \end{cases} \tag{6}$$

Here, $RT(OCT)$ represents the effect of the rototranslation to each OCT frame. The lateral boundary conditions are selected as *natural boundary conditions* (or "do-nothing" boundary conditions) for this problem, so their impact to the final solution is minimal.

The material of the cylinders is assumed to have Young's modulus $E = 0.5$ GPa and Poisson's ratio $\nu = 0$. The Young's modulus does not have a major impact on the solution, mainly driven by the Dirichlet boundary conditions. We tested several values (from 0.5 to 5 GPa with no significant change for the solution on the map). The null Poisson's ratio is selected to prevent any compression or expansion under uni-axial action, to be avoided in this context.

The deformation field obtained by solving the problem (4,6) in Fenics is applied to each vertex of L-view skeleton, to obtain the 3D wireframe of the stent (Fig. 5b). The connectivity of the skeleton is untouched by the map.

To perform this step, it is critical to retrieve the elements of the mesh of the L-view where each vertex of the skeleton belongs to. This is performed by VTK [51]. VTK allows us to find the tetrahedron number of each vertex efficiently.

After the map, the tetrahedron connectivity will be unchanged. Once the element is found, the barycentric coordinates of the vertex (i.e., the system of coordinates relative to the nodes of the tetrahedra) are computed. Notice that the barycentric coordinates are invariant after the mapping. A standard function converting the barycentric coordinates into the Cartesian ones is eventually applied to each vertex of the polyline. The final skeleton is the result of the connectivity applied to the new coordinates.

Post-print

2.2.3 Stent volume reconstruction

The stent 3D volume reconstruction is based on two essential libraries: (a) the spline approximation of the 3D polyline to obtain a smooth representation of the stent skeleton and (b) the volume sweeping along the stent skeleton. The spline approximation of the mapped polylines is performed with OpenCascade, Open Cascade Technology (OCCT) version 7.3 (OPENCASCADE Company, Guyancourt, France). The Computational Geometry Algorithms Library (CGAL) handles the volumetric reconstruction [25].

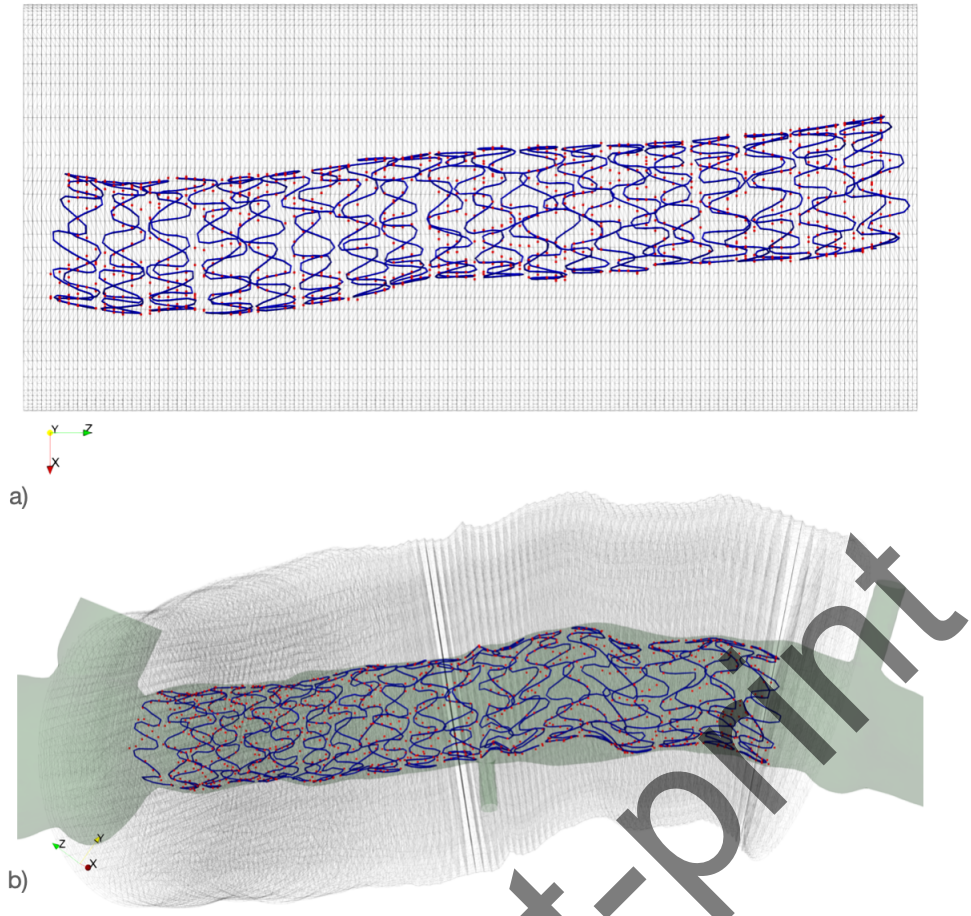

Fig. 5 Test case for a Medtronic Resolute Onyx: a) L-view registered stent polyline (blue) and stent strut point-cloud (red) retrieved by the OCT, embedded in the meshed cylinder; b) final 3D configuration after the mapping in the lumen (green). The deformation field is determined by solving Eqs. (4, 6). Our approach works for any kind of stents, not necessarily a Bioresorbable one, as shown here. The data for depicted case were acquired through the Shear-Stent clinical trial (NCT02098876).

Post-print

Volume sweeping and Nef polyhedra. We reconstructed the 3D stent volume by sweeping the stent cross-section on the centerline. However, in its most basic version this approach may lead to self-intersection problems, preventing a correct meshing.

Following [35], we classify *self-intersections into two categories*. The first type is the *global self-intersection*, see Fig. 6a. Such self-intersections occur where struts are in contact. These contacts are not explicitly handled during the registration process. In practice, they correspond to a mishandled contact between two parts of the strut, with a consequent singularity in the stress at the self-intersection location.

The second type is the so-called *local intersection* that occurs when the curvature of the stent medial axis is too large, concerning the stent cross-sectional diameter[4], see Fig. 6b.

Avoiding or removing self-intersecting triangles is critical to prevent extensive manual corrections of the mesh *a posteriori*. In our current approach, self-intersections are not explicitly excluded during the registration process, e.g., by enforcing mechanical deformations and contact constraints. However, self-intersection removal of free-form surfaces is a difficult problem [52], and most standard commercial CAD packages fail at producing a correct swept surface in such a situation. To this aim, we handle intersections not at the surface but at the mesh level, see Fig. 6. This means that stent swept self-intersecting surfaces are allowed, but the reconstructed surface mesh does not have self-intersecting triangles.

To handle self-intersections a-priori, both local and global, we can consider implicit modeling approaches [23]; for example a tubular structure can be modeled as an infinite union of spheres [41,35] or as an offset surface [5]. The surface of a stent with a circular cross-section is then defined as an infinite union of spheres running along with the stent skeleton. In this way, self-intersections are avoided in the meshing, just combining the spheres in the sweeping process. However, in its original formulation, this approach does not apply to sharp shapes like rectangular ones - as in Absorb GT1 scaffolds. The extension to this case is not trivial and it is one of the novel contributions of the present work, with the introduction of Nef-polyhedra [26].

A Nef-polyhedron is defined as a finite set of Boolean operations of half-planes (see [6], Definition 1). For example, a triangle is the interior of a set of three vertices linked by three straight segments (edges). We may also represent the triangle by the intersection of three half-planes supporting each edge, as in Theorem 7.1.4 in [7][5]. By definition, exact Boolean operations applied to Nef-polyhedra generate a Nef-polyhedra. The library CGAL allows exact computations with Nef-polyhedra [25,27].

Starting from self-intersection free polyhedra, the exact generation of Nef-polyhedra preserves the self-intersecting nature of the final mesh see Fig. 6.

The discrete representation of the final swept surface and the final volume. Following [9], we split the sweeping trajectory into *translation* and *rotation* components, see also Eq. (3). At this point, the swept stent is the result of the infinite union of the cross-sections along the trajectory. The Frenet frame can be sensitive. Stabilized solution might be desirable; see, e.g., [58].

To obtain a discrete representation of the sweep operation, the stent cross-section was mapped at a finite number of points along the sweeping trajectory. The convex hull of the vertices of two consecutive cross-sections defines a volumetric unit (Fig. 6), to handle local self-intersections. This approach is

[4] When the stent does not have a circular cross-section, we intend here the diameter of the smallest pipe enclosing the stent.

[5] Notice that Nef-polyhedron are not restricted to convex polytopes [6].

Post-print

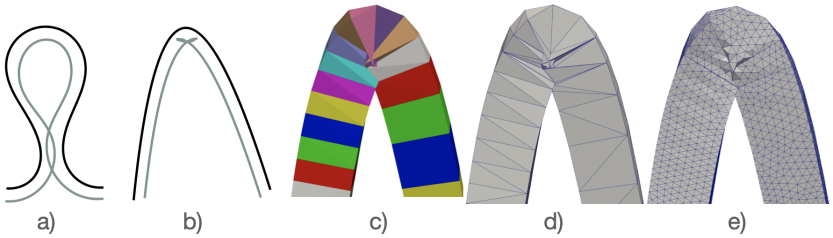

Fig. 6 Self-intersections types and handling: a) global self-intersection; b) local self-intersection; c) stack of slabs showing local self-intersections d) surface after Nef-polyhedron boolean union without self-intersections e) no self-intersection allow for easier mesh computations such as isotropic remeshing of surface d.

limited to convex cross-sections, like the ones commonly found for stents. This limitation has therefore no practical consequences for the purpose of this study.

The stent is then obtained by performing the boolean union of all volumetric units (Fig. 6). It results that for global self-intersections, we simply merge the touching volumes and mesh them as a continuum.

As a last step to retrieve the lumen with the footprint of the stent, we use CGAL as well. Precisely, the 3D stent is subtracted to the unstented lumen with the Polygon Mesh Processing (PMP) package [33]. This package allows for tangential relaxation and local remeshing at the intersection of the lumen and the stent when necessary.

2.3 Computational fluid dynamics

The focus of this paper is on the geometrical reconstruction of the patient-specific stented artery with a high level of automation and minimal manual operations. However, a natural finalization of this reconstruction is the computation of blood flow in the reconstructed geometry. The information retrieved by the CFD may help understanding the interplay between hemodynamics and adverse events of the PCI, as well as potentially supporting prognostic analyses and the design of next-generation scaffolds, in the long-term. We add here some results of CFD with the aim of (i) validating indirectly the efficacy of our geometrical reconstruction, when compared with the CFD in a highly accurate (and time consuming) reconstruction taken here as ground-truth; (ii) providing a proof-of-concept that our method does actually provide a quality mesh for CFD in patient-specific cases. The use of the present methodology on a larger volume of retrospective (and, on a longer term, prospective) clinical data is a natural follow-up of the present work.

In detail, one of the most critical local hemodynamic indexes for the interplay between the stent geometry and the flow patterns is the Wall Shear Stress (WSS) along the luminal surface of the stented coronary artery [44]. The predictive role of the WSS for restenosis or other adverse events in coronary arteries has been clearly pointed out in the literature (see, e.g., [49]).

Post-print

WSS computation was performed here based on the commercial package Fluent (ANSYS Inc., Canonsburg, PA, USA) with a steady-state computation to show the applicability of the method as it would have been with a transient simulation. The steady solver was used as a surrogate of the time average of the unsteady solution. Since we are comparing here two different geometrical reconstruction methods using the same CFD methods, the choice of the surrogate steady solver does not undermine the quality of the results and the cross-validation of the geometrical reconstruction. As a matter of fact, we performed comparisons between the Time-Average WSS on unsteady simulations and the steady WSS (using two different methods and solvers), finding similar results. This is promptly explained by the relatively low Reynolds numbers involved. We do not report this comparison here, for the sake of brevity. Also, we do not consider in this work any new CFD methodology specific for stented arteries, even though special techniques may be in order to accelerate the CFD computations in the future [55].

2.3.1 Stented phantom

The hemodynamics computed in a stented coronary artery phantom, which was previously reconstructed manually and validated by Migliori et al. [36], was compared with the one reconstructed with the proposed semi-automated stent reconstruction method (Fig. 7).

The fluid domains were discretized into tetrahedral elements using ICEM CFD (ANSYS Inc.). The meshes were refined in the proximity of the stent following a previous mesh independence study [13]. The maximum element-size allowed for the Octree meshing algorithm at the strut level is 35 μm, resulting in five to eight elements on each side of the rectangular struts. The parameters and the boundary conditions imposed for the simulation were the same used in [36]. The blood density was set to 1060 kg m^{-3}. A non-Newtonian Carreau rheology was assumed [20]. The inflow boundary condition was set as a constant velocity profile with a steady flow-rate of 45.15 ml/min. This is a typical mean flow-rate value for coronaries (LAD in particular) [30]. A homogeneous pressure condition was prescribed at the outlet. The non-slip condition was applied at the walls, considered as rigid. The maximum Reynolds number was ∼92. For more details on the solver, refer to [8].

2.3.2 Patient-specific cases

In addition to the stented phantom, we performed CFD simulations of the two patient-specific stented cases. Those two patients come retrospectively from the ABSORB-III RCT registry (ClincalTrials.gov NCT01751906) OCT endpoint, which received an Abbott Absorb GT1 bioresorbable scaffold. The two cases were selected because they represented one straight and one curved vessel, showing the versatility of the proposed approach (RM) to model post-intervention patient-specific stents. In this case, an inflow rate of 70.8 ml/min for BVS1 and 102 ml/min for BVS2 with a flat profile was selected to mimic conditions

Post-print

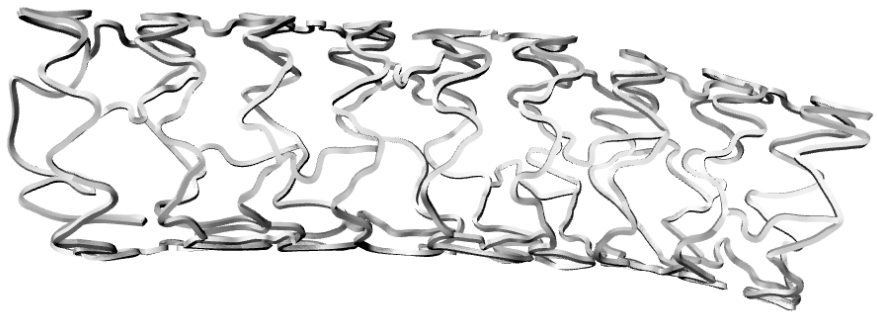

Fig. 7 Multi-Link 8 3D geometry [36]: volumetric reconstruction from the stent skeleton obtained with the proposed sweeping method.

of a moderate exercise, with a Coronary Flow Reserve of 2 [3]. Null traction conditions were prescribed at the outflow.

Post-print

3 Results

3.1 3D Stented Lumen Reconstruction

3.1.1 Skeletonization

The stent skeletonization is tested in both a *qualitative* and a *quantitative* way. The *qualitative* evaluation consists of a direct visual inspection to check if the geometry of the skeleton is coherent with the stent design. The *quantitative* evaluation is performed by measuring D^{SSD} in Equation (2) between the polyline obtained using our anisotropic morphing method and the corresponding OCT-derived point cloud. The smaller this mismatch is, the more accurate the skeletonization is expected to be.

When compared with the literature, our RM anisotropic approach obtains on the phantom of Migliori et al. [36] an optimal difference $D^{SSD} = 76.21$ mm^2. The customized manual method in [36] led to a value $D^{SSD} = 70.77$ mm^2. The accuracy is better for the manual method, but with an acceptable gap ($< 10\%$). *Our method is fully automatic and requires less than an hour (on a personal computer with OS X El Capitan 10.11.6 operating system, processor 1.6 GHz Intel Core i5, 8 GB RAM).* The method in [36] requires about *one day with a significant operator-dependent component.*

Specifically, we evaluate quantitatively two aspects of our approach, (a) the anisotropy in the definition of the distance, when increasing κ; (b) the performance of RM vs. MR.

(a) In Tab. 1, the results for isotropic and anisotropic (with different values of κ) registrations are presented for our phantom.

Table 1 Polyline-to-point-cloud registration: isotropic vs anisotropic $D^{SSD}(mm^2)$ in the Multi-Link 8 Phantom.

κ	1 (Isotr)	3.1	10	31.1	100
$D^{SSD}(mm^2)$	3.39	2.9	2.05	1.92	1.77

Table 2 Polyline-to-point-cloud registration: isotropic vs anisotropic $D^{SSD}(mm^2)$ in BVS1 and BVS2.

BVS1					
κ	1 (Isotr)	3.1	10	31.1	100
$D^{SSD}(mm^2)$	9.43	5.83	3.89	1.64	0.84
BVS2					
κ	1 (Isotr)	3.1	10	31.1	100
$D^{SSD}(mm^2)$	25.15	15.05	10.55	6.28	4.35

In Tab. 2 we present the same results for the two BVS cases. Notice that the noise was much higher in BVS2, leading to a larger D^{SSD} than for the other cases.

(b) The results of the RM and MR methods are compared in Tab. 3. We illustrate the skeletons of the three cases in Fig. 8a,b,c.

Post-print

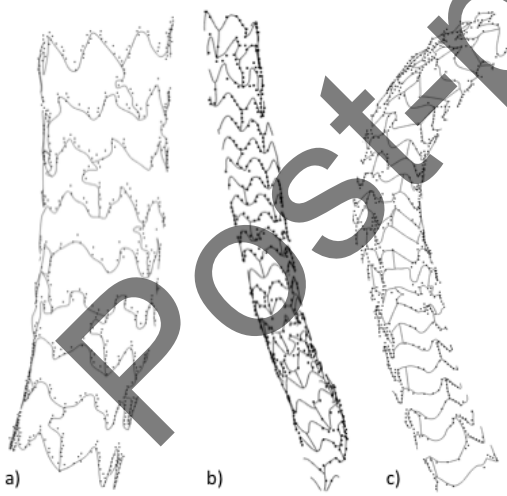

Fig. 8 Skeletons of the Multi-Link 8 phantom case (a), BVS1 case (b) and BVS2 case (c) obtained with the RM method. Half stents (anterior part) are shown for visualization purposes.

Table 3 Stent skeletonization: comparison of MR vs RM.

CASE	D_{MR}^{SSD} (mm^2)	D_{RM}^{SSD} (mm^2)
Multi-Link 8 phantom	7.48	2.05
BVS1	10.19	3.89
BVS2	20.30	10.55

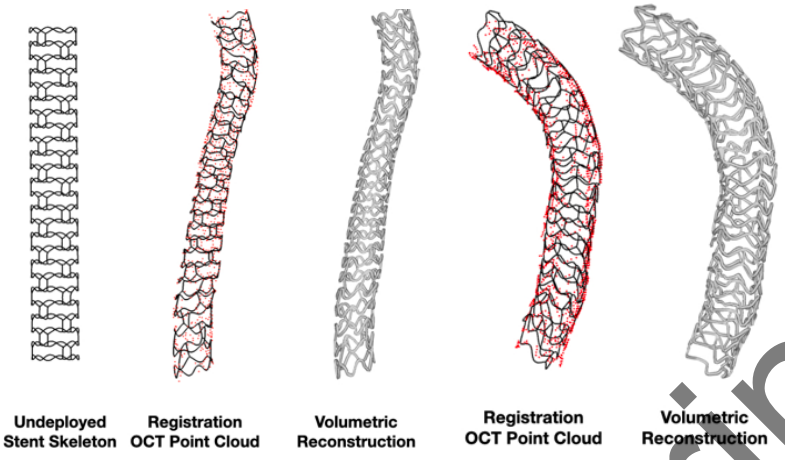

Fig. 9 OCT-based construction process from the undeployed stent, and OCT point cloud (red dots) registration, to the 3D Stent. Left: The Undeployed Stent Skeleton. Center (second and third panels): BVS1. Right (fourth and fifth panels): BVS2.

Post-print

3.1.2 Stent volume reconstruction

Figure 9 shows the final 3D reconstruction of the bioresorbable scaffold of one patient-specific case (BVS2). *The entire volumetric reconstruction process takes from 10 to 30 minutes (depending on the stent model and length) on a desktop workstation (an 8 3.2GHz cores Intel Xeon* 10^{th} *generation, 32GB Ram).* The volumetric reconstruction time depends primarily on the length of the stent and the complexity of the cross-section. The reconstruction method was able to handle the reconstruction of both straight and curved stent geometries, as highlighted in Fig. 9, which depicts the final 3D reconstruction of BVS1 and BVS2, respectively.

The expected overall turnaround time, i.e., including lumen/strut segmentation, image registration, 3D mapping, and volume reconstruction, of the preparation of the geometry, was around 4 hours. Out of these hours, the workflow from the registration through the meshing required - the specific suhourect of the present work - required less than an hour.

3.2 Computational fluid dynamics

Stented phantom Figure 10 compares the WSS contours (left) and the stented lumen surface where WSS was lower or equal to 0.4 Pa (right) for the two cases. Luminal regions with low WSS, i.e., with WSS lower than 0.4 Pa, are of interest as they are susceptible to develop atherosclerosis [34]. The WSS distributions were in good agreement.

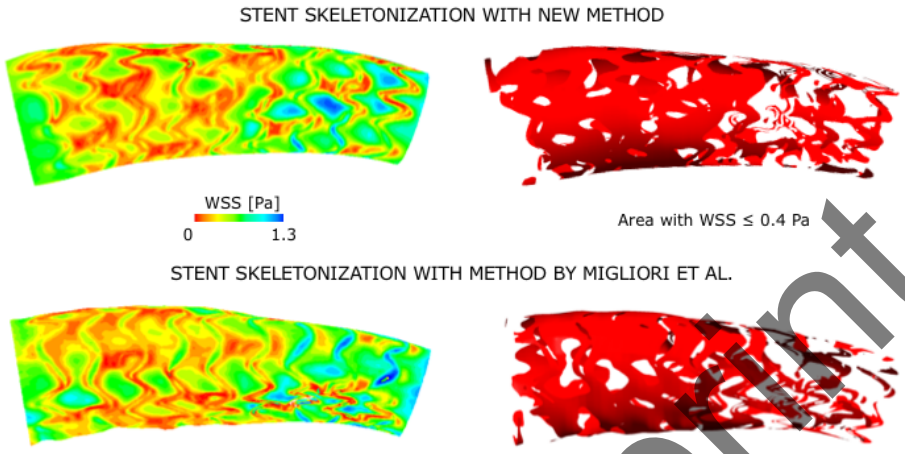

Fig. 10 Hemodynamic results with the new method (middle) and that proposed by Migliori et al. [36] (bottom): contour maps of WSS (left); stented lumen surface exposed to WSS $\leq$ 0.4 Pa (right).

Post-print

The mean WSS (denoted by $\overline{WSS}$) was calculated for both models as

$$\overline{WSS} \equiv \sum_{i=1}^{N} WSS_i \frac{A_i}{A} \tag{7}$$

where A is the total area of the stented portion of the lumen, N is the total number of elements of the stented lumen surface, WSS_i is the WSS on the ith element, which has area A_i. The obtained values were 0.439 Pa in the case with the stent reconstructed with the new method and 0.448 Pa in the case in [36] with a 2% difference. Furthermore, the percentage of stented lumen surface exposed to WSS lower than 0.4 Pa was calculated for both cases as

$$lowWSSarea = \frac{A_{WSS \leq 0.4}}{A} \times 100 \tag{8}$$

where $A_{WSS \leq 0.4}$ is the portion of stented lumen area with WSS $\leq$ 0.4 Pa (this area is highlighted with the red surfaces on the right in Fig. 10). The

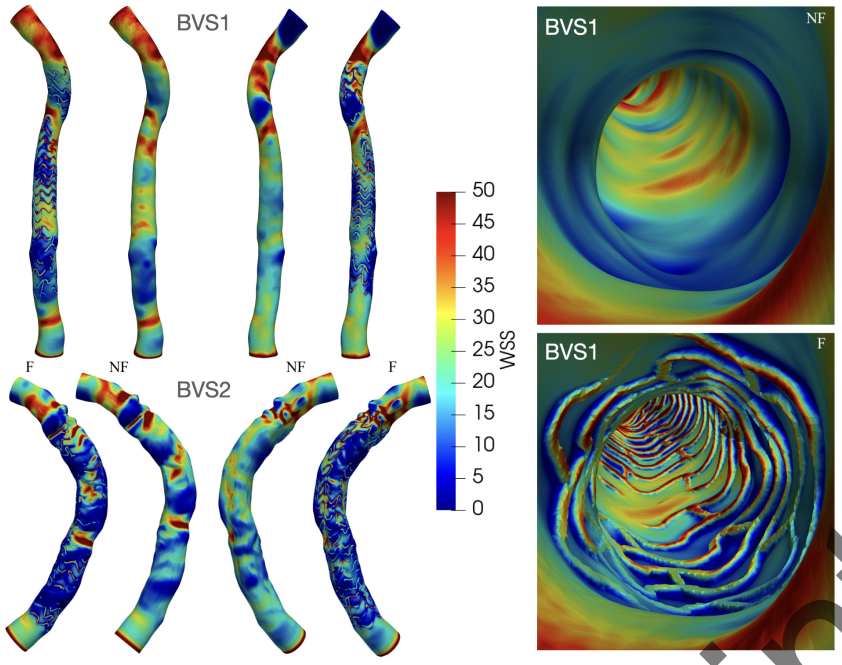

Fig. 11 Comparison of the WSS computed with the Footprint (F) of the stent and without it, i.e., No-Footprint (NF). At the top left, BVS1, on the bottom left, BVS2, right: inner view for BVS1.

obtained values were 49.92% in the case with the stent reconstructed with the new method and 49.15% in the case in [36], with a 1.5% difference.

Patient-specific cases Figure 11 shows the comparison between the WSS computed with and without the footprint of the stent (marked by F and NF, respectively). The local differences in the WSS maps are apparent.

4 Discussion

To obtain a mathematical representation of a patient-specific stented coronary artery, two approaches are possible. In the "model-driven" approach, one performs the simulation of the deployment in the patient-specific lumen. This approach, by construction, is certainly consistent with the physics of the problem, as the virtual deployment obeys physical principles [14]. This approach is also "predictive", as it potentially allows to anticipate prospectively the deployment results. However, it suffers from a substantial lack of patient-specific knowledge of the arterial wall's material properties and the parameters of the constitutive laws that describe, for instance, the contact between the stent struts and the arterial wall.

Post-print

On the other hand, a purely "data-driven" approach is also problematic, as the images' geometrical reconstruction reflects the limitations of the imaging tools in terms of resolution and noise. Mathematical techniques intended to "fill the gaps" of the data need several manual adjustments, and not necessarily lead to solutions consistent with the physics [61]. This suggests a "hybrid" approach, where the available data from images are merged with the undeployed design of the stent by image-registration. Image registration was proposed for OCT-based reconstruction in [45,18]; our approach differs for the specific registration methodology [32] and the subsequent skeletonization procedures.

A qualitative comparison among the different approaches is summarized in Tab. 4. The third column refers to our approach.

	Model-Driven	Data-Driven	Data-Assimilation/CAD
Data Noise	No	Yes	Mitigated
Mechanics Parameters	Yes	No	Optional
Wall/Stent Contact	Yes	No	No
Automation	High	Low	High

Table 4 Comparison of pros and cons of different approaches for the stent reconstruction. The last column refers to the present Data-Assimilation/CAD approach presented in this paper. The noise of the data, in this case, is partially fixed by the image-registration and the associated regularization. The regularization in our work does not use any specific information of the mechanics of the stent, but in principle it may take advantage from this knowledge. So, the knowledge of these data is optional, while it is necessary in the model-driven approach.

Post-print

The Registration procedure A hybrid procedure requires a reliable source of data. Here, we combine two sources of images, namely OCT and angiography. OCT imaging is the right candidate for both the transverse and interframe resolutions [47], guaranteeing an appropriate level of accuracy for the size of the struts of 80 μm and 150 μm of metallic and bioresorbable stents, respectively. This allows struts detection on each OCT slice in a semi-automatic way [11,61, 17]. Once the struts are detected, and a cloud of points with their center of mass is formed, the creation of topology is required (skeletonization). Our skeletonization consists of the polyline-to-point registration, previously introduced in [32]. The registration procedure is automatic and operator-independent. Additionally, it fixes problems such as the presence of the guidewire shadow in the OCT images by filling the gaps due to the sparsity of the data.

A specific discussion deserves the selection of the parameter κ for the anisotropic registration. The results of Tab. 1 pinpoint the efficacy of the anisotropic strategy. As expected, the difference D^{SSD} decreases when κ increases, showing that the convergence solution's final distance gets better. However, the presence of the noise can make a too strict adherence to the points nonphysical. Also, the sensitivity of D^{SSD} on κ significantly decreases for $\kappa \geq 10$. The choice for κ can be driven primarily by the ratio of the longitudinal resolution (i.e., interframe distance) and the in-plane resolution. For

the Optis OCT system, this relative resolution is either 20 or 10, depending on the pullback mode and considering an in-plane resolution of $10\mu m$.

In the case of BVS geometries (Tab. 2), the difference between the longitudinal and in-plane resolution is higher, and the noise affecting the images is more pronounced in the longitudinal direction. The dependence of D^{SSD} on κ is more evident (approximated by a regression line with slope -0.18 for BVS1 and -0.28 for BVS2). As previously pointed out, a larger κ may be beneficial to the mismatch, yet the enforcement of a very small D^{SSD} on noisy data conflicts with the physical consistency for the relative motion of the lumen with respect to the OCT catheter during pullback [24].

The 3D Mapping The fusion of OCT images with two angiographic views enables obtaining the 3D patient-specific topology of the stent. The mapping between the L-view of the OCT pullback and the 3D-view presents some technical challenges. In fact, the bi-planar angiographies allow the direct construction of the mapping between the catheter and the real vessel centerline only in the frames corresponding to OCT slices. How this deformation extends to all the skeleton obtained after the registration requires some specific method. Available manual strategies [12] are generally operator-dependent and time consuming. Here, we resort to a method based on *computational mechanics*. The elasticity model (4,6) is used for retrieving the L-view/3D- view map. Therefore, the quantitative impact of the model parameters on the final result is minimal. Our approach can be classified as RM (Register-then-Map) so that the skeleton is first computed in the L-view and then mapped to the 3D frame. Another option is possible, namely MR (Map-then-Register), in which the points from the OCT are mapped to the 3D, and eventually, the image registration is performed to retrieve the 3D skeleton directly. We compared the two approaches in Tab. 3. The RM approach gives a pay-off when compared with the more immediate MR workflow when we consider the value of the difference D^{SSD} attained by the RM approach. As reported in Tab. 3, the RM results were better in all the tested cases, with reductions of the final errors of 68.85% in the Multi-Link 8 phantom case, of 60.35% in the BVS1 case and of 47.59% in the BVS2 case. These results can be mainly motivated by the following two reasons.

(i) The registration to the 3D view is more prone to sub-optimal solutions. This means that the minimization intrinsic to the registration can be more effective in the L-view than in the 3D, for the variety and complexity of the different possible configurations in the patient framework. To mitigate the risk of being trapped in local minima, the regularization term needs to be carefully calibrated, as recommended in [32].

(ii) Working in the L-view frame for the registration allows the anisotropic approach, as the OCT-resolution is different in directions that correspond to the Cartesian ones only in the L-view.

Our *final recommendation* based on these results is *to pursue the RM anisotropic approach.*

Post-print

Volume reconstruction of the Stent The volume reconstruction of the stent from the skeleton is troublesome for possible inconsistencies leading to "self-intersections" of the final surface triangulation. Self-intersections are singularities of the curves representing the surface and significantly undermine the meshing process for CFD [35]. To avoid this problem, we presented an automatic and robust stent volume reconstruction based on Nef-polyhedra. This computational geometry concept allowed the automatic reconstruction of the volume with a sequence of Boolean operations. This allowed the creation of conformal meshes of both the lumen and the stent that guaranteed the correctness of the final volumetric mesh of the stented lumen for CFD computations.

CFD Analysis To assess the accuracy of our approach, we tested it on a phantom introduced in [36], as well as on two patient-specific geometries from the Emory University Hospital with a bioresorbable scaffolds. The choice of bioresorbable scaffolds was motivated by the interest triggered by the frequency of adverse events for these devices, possibly related by the local hemodynamics induced by the struts, whose thickness is larger than for classical Drug-Eluting Stents.

The novel methodology presented here obtained accurate 3D models of stented coronary arteries, useful for quantitative analyses, including CFD simulations. Precisely, the semi-automatic procedure presented here can compute a CFD analysis within 5 hours (from DICOM to CFD results) as opposed to the manual procedure, requiring order of days of work (not to mention operator-dependence).

The results of Fig. 11 pinpoint the importance of the stent footprint into the CFD analysis. We speculate that in the hemodynamics of stented arteries there are two major geometrical factors affecting the WSS distribution in a stented artery: (i) the centerline curvature (bending and torsion), that we identify as a "non-local" factor; (ii) the presence of the struts, that we call a "local" factor. The two factors overlap and seem to be both decisive in the final WSS distribution. For instance, looking at the BVS1 results, it is evident that where the struts are absent or the artery has a significant bending (top of BVS1), the WSS distributions in the F and NF are similar, while they differ significantly for the presence of struts. More specifically, the struts seem to reduce the WSS and likely increment its oscillations. This may provide an explanation to the occurrence of adverse events. These speculations need to be confirmed on a larger number of cases.

Timing The primary driver of the overhaul size of the registration problem is the stent length, as discussed above. Consequently, longer stents will require more time to process. For stents about 40 mm long, our experience, on an 8 3.2GHz cores Intel Xeon 10^{th} generation and our current implementation, is as follows: registration 10 minutes, 3D mapping 30 minutes, volumetric reconstruction 20 minutes. Regarding timing of the CFD simulations, the results depend significantly on the simulation type and mesh accuracy required. Our timing experience ranged from 1 hour with Fluent and a coarse grid for a steady simulation on a modern

Post-print

workstation to 48 hours with finite elements and LifeV, a fine grid on an HPC cluster (Stampede2 at Texas Advanced Computing Center with 192 cores).

Limitations The work features limitations and room for improvement.

1. The first improvement lies in the stent strut-detection on the OCT-images, where we can significantly accelerate by incorporating machine learning algorithms for the completely automatic detection of the struts. This is anticipated to significantly shorten the turnaround time.
2. In the polyline-to-point cloud registration the penalization, that currently includes only stretching, is not derived from a specific constitutive laws. An adequate *rod modeling*, including the penalization of bending and twisting modes, might further improve the stent skeleton morphing process.
3. An alternative procedure for the volumetric reconstruction is to obtain the volume directly in the L-view and then to use our mapping for the final 3D reconstruction. This approach will be considered in future work.
4. We need to improve our knowledge of some parameters, in particular, κ and its interplay with the parameters of the registration procedure. An optimal selection of this parameter may eventually rely on statistical or machine learning algorithms.

The present results do not include side-branches in the coronary. This is not a limitation of the stent registration and reconstruction that we propose here. The inclusion of the side-branches attains the lumen reconstruction and the prescription of boundary conditions for the CFD analysis. Once these steps can be done, our stent reconstruction method applies promptly.

As a follow-up research, we also mention the extensive quantitative comparison of different approaches, beyond Tab. 4. This would require the introduction of a common benchmark with an accurate identification of the ground truth, where different approaches could be probed in terms of accuracy and efficiency/automation.

Post-print

5 Conclusions

In this work, we introduced a sequence of steps that lead to an accurate reconstruction of stented coronary artery models from OCT and angiographic data in a relatively short timeline. This may enable the patient-specific hemodynamic analysis of small clinical studies based on OCT acquisitions.

The *novelty* of our reconstruction approach lies in (i) the *combination of modeling-based procedures and data assimilation, with the help of advanced mathematical tools like point-to-polyline registration*; (ii) the *L-view/3D mapping based on elasticity*, with a Registration-then-Map workflow motivated by the results; (iii) the stent implicit modeling for the volumetric reconstruction based on *Nef-polyhedra*.

It is important to stress that *the computational time for these three steps leading from the point-cloud to the stented geometry fits within an hour with a high level of automation*. As a future development of the present work, we

plan to improve the strut detection on the images and the corresponding segmentation, with a semi-automatic (possibly Machine-Learning based) pattern recognition to accelerate the identification of the shapes of the struts.

Nevertheless, our *results* gave confidence that our approach provides usable (reliable and efficient) tools for comprehensive investigations. In addition, the presented and cross-validated CFD simulations demonstrated that reliable maps of WSS could be obtained within a few hours. This turnaround time allows to process a number of patients compatible with small retrospective studies (order of tenths or few hundreds cases). To the best of authors' knowledge, state-of-art methodologies were used so far to process just a few patients [18, 45]. Small retrospective studies may allow to identify quantitative relations between adverse events and the local hemodynamics that could eventually feed larger (retrospective and prospective) clinical trials. The identification of one or more common benchmarks for testing different approaches is also a desirable step, for a precise assessment of the different options [60].

When comparing cases with and without the footprint of the stents, it is apparent that the WSS maps are significantly affected by the presence of the stent struts, demonstrating that an accurate patient-specific reconstruction of the stented artery is mandatory for any clinical analysis. Small clinical studies may help confirming/rejecting this statement and the procedure presented here provides a significant improvement in the image/geometry processing required by the CFD. The current development of our methodology aims to shorten the turnaround time to fit within 2 hours, with a high level of operator independence (so to engage an operator for less than one hour). This may potentially enable these tools for larger clinical studies.

Finally, we mention that the proposed procedure can be used for 3D printing of post-deployment patient-specific geometries.

Acknowledgements The contribution of Boyi Yang and Gaetano Esposito (Emory University Hospital) to the early stages of this work is gratefully acknowledged. S. B. thanks the Department of Mathematics at Emory University for the hospitality. A.V., H.S., D.M. and A.L. thank Don Giddens for many fruitful discussions on the topics of the paper and suggestions when preparing the manuscripts.

Post-print

Declarations

Funding

Some of the computation were performed on XSEDE facilities (Stampede 2) under the NSF-XSEDE TG-ASC160069 Grant.

H. S. acknowledges the support to his research from Medtronic, Abbott Vascular, Philips, Gilead.

Conflict of interest/Competing interests

The authors Adrien Lefieux, Sara Bridio, David Molony, Marina Piccinelli, Claudio Chiastra, Francesco Migliavacca declare that they have no conflict of interest.

H. Samady and A. Veneziani are co-founders, former CMO/consultant and CSO respectively and equity holders of COVANOS Inc. A. Lefieux is a consultant and equity holder of COVANOS Inc. No conflict of interest to be disclosed for this activity.

H. S. received grants from Medtronic, Abbott Vascular, Philips, Gilead

H. Samady is also part of the Trial steering committee, consultant for Philips, Abbott Vascular.

Availability of data and material

The codes developed for this paper are under GPL Licence and will be available upon request to the corresponding author.

The data used for benchmarking can be requested as well.

Authors' contributions

A.L.: method design, development, advising, code implementation, paper writing. S.B.: method design, development, code implementation, paper writing. M.P.: code development, paper writing. D.M.: data collection, image segmentation, proofreading. H.S.: clinical direction, data collection, supervision and handling of the clinical data, proofreading. C.C.: F.M.: method design, advising, results analysis, proofreading. A.V.: method design, advising, results analysis, paper writing.

Ethics approval/Consent to participate

No human studies were carried by the authors specifically for this paper. Anonymized patient data used in this study were existing data collected using approved protocol with informed consent obtained.

Consent for publication

All the authors approve the content of the paper and its publication.

Post-print

References

1. Alnæs, M.S., Blechta, J., Hake, J., Johansson, A., Kehlet, B., Logg, A., Richardson, C., Ring, J., Rognes, M.E., Wells, G.N.: The fenics project version 1.5. Archive of Numerical Software **3**(100), 9–23 (2015)
2. Antiga, L., Ene-Iordache, B., Remuzzi, A.: Computational geometry for patient-specific reconstruction and meshing of blood vessels from mr and ct angiography. IEEE transactions on medical imaging **22**(5), 674–684 (2003)
3. Barash, P.G.: Clinical anesthesia. Lippincott Williams & Wilkins (2009)
4. Barquera, S., Pedroza-Tobías, A., Medina, C., Hernández-Barrera, L., Bibbins-Domingo, K., Lozano, R., Moran, A.E.: Global overview of the epidemiology of atherosclerotic cardiovascular disease. Archives of medical research **46**(5), 328–338 (2015)
5. Berger, M., Gostiaux, B.: Géométrie différentielle, variétés, courbes et surfaces. Press Universitaire de France (1987)
6. Bieri, H.: Nef polyhedra: A brief introduction. In: Geometric modelling, pp. 43–60. Springer (1995)
7. Boissonnat, J.D., Yvinec, M.: Algorithmic geometry. Cambridge university press (1998)
8. Bridio, S.: An Innovative Method For Automatic Image-based Patient-specific Stent Reconstruction For Computational Fluid Dynamics Analyses. Master's thesis, Politecnico di Milano, Italy (2018)
9. Campen, M., Kobbelt, L.: Polygonal boundary evaluation of minkowski sums and swept volumes. Eurographics Symposium on Geometry Processing **29**(2), 1613–1622 (2010)
10. Chiastra, C., Dubini, G., Migliavacca, F.: Hemodynamic perturbations due to the presence of stents. In: Biomechanics of Coronary Atherosclerotic Plaque, pp. 257–278. Elsevier (2020)
11. Chiastra, C., Migliori, S., Burzotta, F., Dubini, G., Migliavacca, F.: Patient-specific modeling of stented coronary arteries reconstructed from optical coherence tomography: Towards a widespread clinical use of fluid dynamics analyses. Journal of cardiovascular translational research pp. 1–17 (2017)
12. Chiastra, C., Montin, E., Bologna, M., Migliori, S., Aurigemma, C., Burzotta, F., Celi, S., Dubini, G., Migliavacca, F., Mainardi, L.: Reconstruction of stented coronary arteries from optical coherence tomography images: Feasibility, validation, and repeatability of a segmentation method. PloS one **12**(6), e0177495 (2017)
13. Chiastra, C., Morlacchi, S., Gallo, D., Morbiducci, U., Cárdenes, R., Larrabide, I., Migliavacca, F.: Computational fluid dynamic simulations of image-based stented coronary bifurcation models. Journal of The Royal Society Interface **10**(84), 20130193 (2013)
14. Chiastra, C., Wu, W., Dickerhoff, B., Aleiou, A., Dubini, G., Otake, H., Migliavacca, F., LaDisa Jr, J.F.: Computational replication of the patient-specific stenting procedure for coronary artery bifurcations: From oct and ct imaging to structural and hemodynamics analyses. Journal of biomechanics **49**(11), 2102–2111 (2016)
15. Cho, H.S., Jang, S.J., Kim, K., Dan-Chin-Yu, A.V., Shishkov, M., Bouma, B.E., Oh, W.Y.: High frame-rate intravascular optical frequency-domain imaging in vivo. Biomedical optics express **5**(1), 223–232 (2014)
16. Dey, T.K.: Curve and Surface Reconstruction. Cambridge University Press (2006)
17. Elliott, M.R., Kim, D., Molony, D.S., Morris, L., Samady, H., Joshi, S., Timmins, L.H.: Establishment of an automated algorithm utilizing optical coherence tomography and micro-computed tomography imaging to reconstruct the 3d deformed stent geometry. IEEE Transactions on Medical Imaging (2018)
18. Ellwein, L.M., Otake, H., Gundert, T.J., Koo, B.K., Shinke, T., Honda, Y., Shite, J., LaDisa, J.F.: Optical coherence tomography for patient-specific 3d artery reconstruction and evaluation of wall shear stress in a left circumflex coronary artery. Cardiovascular Engineering and Technology **2**(3), 212 (2011)
19. Engl, H.W., Hanke, M., Neubauer, A.: Regularization of inverse problems, vol. 375. Springer Science & Business Media (1996)
20. Formaggia, L., Quarteroni, A., Veneziani, A.: Cardiovascular Mathematics: Modeling and simulation of the circulatory system, vol. 1. Springer Science & Business Media (2010)

Post-print

21. Geuzaine, C., Remacle, J.F.: Gmsh: A 3-d finite element mesh generator with built-in pre-and post-processing facilities. International journal for numerical methods in engineering **79**(11), 1309–1331 (2009)
22. Gogas, B.D., King, S.B., Timmins, L.H., Passerini, T., Piccinelli, M., Veneziani, A., Kim, S., Molony, D.S., Giddens, D.P., Serruys, P.W., et al.: Biomechanical assessment of fully bioresorbable devices. JACC: Cardiovascular Interventions **6**(7), 760–761 (2013)
23. Gomes, A., Voiculescu, I., Jorge, J., Wyvill, B., Galbraith, C.: Implicit curves and surfaces: mathematics, data structures and algorithms. Springer Science & Business Media (2009)
24. Ha, J.: Physical principles and equipment of intravascular optical coherence tomography. In: Coronary Imaging and Physiology, pp. 97–106. Springer (2018)
25. Hachenberger, P., Kettner, L.: 3D boolean operations on nef polyhedra. In: CGAL User and Reference Manual, 4.13.2 edn. CGAL Editorial Board (2019)
26. Hachenberger, P., Kettner, L., Mehlhorn, K.: Boolean operations on 3d selective nef complexes: Data structure, algorithms, optimized implementation and experiments. Computational Geometry **38**(1-2), 64–99 (2007)
27. Hachenberger, P., Kettner, L., Mehlhorn, K.: Boolean operations on 3d selective nef complexes: Data structure, algorithms, optimized implementation and experiments. Computational Geometry **38**(1-2), 64–99 (2007)
28. Jang, S.J., Park, H.S., Song, J.W., Kim, T.S., Cho, H.S., Kim, S., Bouma, B.E., Kim, J.W., Oh, W.Y.: Ecg-triggered, single cardiac cycle, high-speed, 3d, intracoronary oct. JACC: Cardiovascular Imaging **9**(5), 623–625 (2016)
29. Katwal, A.B., Lopez, J.J.: Technical considerations and practical guidance for intracoronary optical coherence tomography. Intravascular imaging: OCT and IVUS, an issue of interventional cardiology clinics **4**, 239–250 (2015)
30. Kessler, W., Moshage, W., Galland, A., Zink, D., Achenbach, S., Nitz, W., Laub, G., Bachmann, K.: Assessment of coronary blood flow in humans using phase difference mr imaging. comparison with intracoronary doppler flow measurement. International journal of cardiac imaging **14**(3), 179–86 (1998)
31. Kilic, Y., Safi, H., Bajaj, R., Serruys, P.W., Kitslaar, P., Ramasamy, A., Tufaro, V., Onuma, Y., Mathur, A., Torii, R., et al.: The evolution of data fusion methodologies developed to reconstruct coronary artery geometry from intravascular imaging and coronary angiography data: a comprehensive review. Frontiers in Cardiovascular Medicine **7** (2020)
32. Lin, C.Y., Veneziani, A., Ruthotto, L.: Numerical methods for polyline-to-point-cloud registration with applications to patient-specific stent reconstruction. International journal for numerical methods in biomedical engineering **34**(3), e2934 (2018)
33. Loriot, S., Tournois, J., Yaz, I.O.: Polygon mesh processing. In: CGAL User and Reference Manual, 4.13.2 edn. CGAL Editorial Board (2019)
34. Malek, A.M., Alper, S.L., Izumo, S.: Hemodynamic shear stress and its role in atherosclerosis. Jama **282**(21), 2035–2042 (1999)
35. Meakawa, T., Patrikalakis, N., Sakkalis, T., Yu, G.: Analysis and applications of pipe surfaces. Computer Aided Design Geometric Design **15**, 437–458 (1998)
36. Migliori, S., Chiastra, C., Bologna, M., Montin, E., Dubini, G., Aurigemma, C., Fedele, R., Burzotta, F., Mainardi, L., Migliavacca, F.: A framework for computational fluid dynamic analyses of patient-specific stented coronary arteries from optical coherence tomography images. Medical Engineering and Physics **47**, 105–116 (2017)
37. Migliori, S., Chiastra, C., Bologna, M., Montin, E., Dubini, G., Genuardi, L., Aurigemma, C., Mainardi, L., Burzotta, F., Migliavacca, F.: Application of an oct-based 3d reconstruction framework to the hemodynamic assessment of an ulcerated coronary artery plaque. Medical Engineering & Physics (2020)
38. Migliori, S., Rampat, R., Bologna, M., Montin, E., Burzotta, F., Hildick-Smith, D., Dubini, G., Mainardi, L., Migliavacca, F., Cockburn, J., et al.: A patient-specific study investigating the relation between coronary hemodynamics and neo-intimal thickening after bifurcation stenting with a polymeric bioresorbable scaffold. Applied Sciences **8**(9), 1510 (2018)
39. Modersitzki, J.: Numerical methods for image registration. Oxford University Press on Demand (2004)

Post-print

40. Modersitzki, J.: FAIR: flexible algorithms for image registration, vol. 6. SIAM (2009)
41. Monge, G.: Application de l'analyse a la géométrie: a l'usage de l'École impériale polytechnique. Bernard (1807)
42. Myronenko, A., Song, X.: Point set registration: Coherent point drift. IEEE transactions on pattern analysis and machine intelligence **32**(12), 2262–2275 (2010)
43. Nammas, W., Ligthart, J.M., Karanasos, A., Witberg, K.T., Regar, E.: Optical coherence tomography for evaluation of coronary stents in vivo. Expert review of cardiovascular therapy **11**(5), 577–588 (2013)
44. Ng, J., Bourantas, C.V., Torii, R., Ang, H.Y., Tenekecioglu, E., Serruys, P.W., Foin, N.: Local hemodynamic forces after stenting: implications on restenosis and thrombosis. Arteriosclerosis, thrombosis, and vascular biology **37**(12), 2231–2242 (2017)
45. O'Brien, C.C., Kolandaivelu, K., Brown, J., Lopes, A.C., Kunio, M., Kolachalama, V.B., Edelman, E.R.: Constraining oct with knowledge of device design enables high accuracy hemodynamic assessment of endovascular implants. PLoS One **11**(2), e0149178 (2016). DOI 10.1371/journal.pone.0149178
46. Phipps, J.E., Hoyt, T., Halaney, D.L., Mancuso, J.J., Milner, T.E., Feldman, M.D.: Intravascular oct imaging artifacts. In: Cardiovascular OCT Imaging, pp. 67–79. Springer (2015)
47. Prati, F., Jenkins, M., Di Giorgio, A., Rollins, A.: Intracoronary optical coherence tomography, basic theory and image acquisition techniques. The international journal of cardiovascular imaging **27**(2), 251–258 (2011)
48. Sakamoto, A., Jinnouchi, H., Torii, S., Virmani, R., Finn, A.: Understanding the impact of stent and scaffold material and strut design on coronary artery thrombosis from the basic and clinical points of view. Bioengineering **5**(3), 71 (2018)
49. Samady, H., Eshtehardi, P., McDaniel, M.C., Suo, J., Dhawan, S.S., Maynard, C., Timmins, L.H., Quyyumi, A.A., Giddens, D.P.: Coronary artery wall shear stress is associated with progression and transformation of atherosclerotic plaque and arterial remodeling in patients with coronary artery disease. Circulation **124**(7), 779–788 (2011)
50. Sangalli, L.M., Secchi, P., Vantini, S., Veneziani, A.: Efficient estimation of three-dimensional curves and their derivatives by free-knot regression splines, applied to the analysis of inner carotid artery centrelines. Journal of the Royal Statistical Society: Series C (Applied Statistics) **58**(3), 285–306 (2009)
51. Schroeder, W.J., Lorensen, B., Martin, K.: The visualization toolkit: an object-oriented approach to 3D graphics. Kitware (2004)
52. Seong, J.K., Elber, G., Kim, M.S.: Trimming local and global self-intersections in offset curves/surfaces using distance maps. Computer Aided Design **38**, 183–193 (2006)
53. Sethian, J.A.: Level set methods and fast marching methods: evolving interfaces in computational geometry, fluid mechanics, computer vision, and materials science, vol. 3. Cambridge university press (1999)
54. Tagliasacchi, A., Delame, T., Spagnuolo, M., Amenta, N., Telea, A.: 3d skeletons: A state-of-the-art report. In: Computer Graphics Forum, vol. 35 (2), pp. 573–597. Wiley Online Library (2016)
55. Viguerie, A., Veneziani, A.: Deconvolution-based stabilization of the incompressible navier–stokes equations. Journal of Computational Physics **391**, 226–242 (2019)
56. Villiger, M., Ren, J., Uribe-Patarroyo, N., Bouma, B.E.: Future development. In: Cardiovascular OCT Imaging, pp. 175–191. Springer (2020)
57. Wang, J., Jin, X., Huang, Y., Ran, X., Luo, D., Yang, D., Jia, D., Zhang, K., Tong, J., Deng, X., et al.: Endovascular stent-induced alterations in host artery mechanical environments and their roles in stent restenosis and late thrombosis. Regenerative biomaterials **5**(3), 177–187 (2018)
58. Wang, W., Jüttler, B., Zheng, D., Liu, Y.: Computation of rotation minimizing frames. ACM Transactions on Graphics (TOG) **27**(1), 1–18 (2008)
59. Wu, W., Samant, S., de Zwart, G., Zhao, S., Khan, B., Ahmad, M., Bologna, M., Watanabe, Y., Murasato, Y., Burzotta, F., et al.: 3d reconstruction of coronary artery bifurcations from coronary angiography and optical coherence tomography: feasibility, validation, and reproducibility. Scientific reports **10**(1), 1–11 (2020)
60. Wu, W., Sharzehee, M., Zhao, S., Samant, S., Watanabe, Y., Murasato, Y., Mickley, T., Bicek, A., Bliss, R., Burzotta, F., et al.: 3d reconstruction of coronary artery stents from

Post-print

optical coherence tomography: Experimental validation and clinical feasibility. Scientific Reports **11** (2021)
61. Yang, B., Piccinelli, M., Esposito, G., Han, T., Bouchi, Y., Gogas, B., Giddens, D., Samady, H., Veneziani, A.: Patient-specific 3d volumetric reconstruction of bioresorbable stents: A method to generate 3d geometries for computational analysis of coronaries treated with bioresorbable stents. arXiv preprint arXiv:1810.03270 (2018)

Post-print